nature communications

Article

https://doi.org/10.1038/s41467-025-66348-w

Operation of a high-frequency, phase-slip qubit

Received: 3 October 2025

Accepted: 5 November 2025

Published online: 12 December 2025

Check for updates

Cheeranjeev Purmessur[1], Kaicheung Chow[2], Bernard van Heck[3] & Angela Kou[1,2,4]

Aluminum-based Josephson junctions are currently the main sources of nonlinearity for control and manipulation of superconducting qubits. A constriction-based junction provides an alternative source of nonlinearity that promises new types of protected qubits and the possibility of high-temperature and high-frequency operation through the use of superconductors with larger energy gaps. Junctions made from such superconductors have been challenging to incorporate into superconducting qubits because of difficulty controlling junction parameters and have had extremely low lifetimes, which limited their utility. Here we demonstrate that junctions made using titanium nitride (TiN) are a promising and controllable qubit platform. We use TiN junctions to build superconducting qubits based on quantum phase slips through the junction. We operate the qubit at zero flux where the qubit frequency (~ 17GHz) is mainly determined by the inductance of the qubit. We perform readout and coherent control of the superconducting qubit, and measure qubit lifetimes >60μs. Finally, we demonstrate operation of the qubit at temperatures exceeding 300 mK. Our results add the TiN-based junction as a tool for superconducting quantum information processing and opens avenues for new classes of superconducting qubits.

Aluminum-based Josephson junctions (JJ) are the workhorse of superconducting circuits and are the basis of a multitude of useful quantum devices such as quantum-limited amplifiers, single-photon detectors, and superconducting qubits[1–5]. In these devices, superconducting junctions are modeled as tunneling elements for Cooper pairs or as tunneling elements for flux quanta, depending on their impedance environment. The beneficial nonlinearity arising from flux quanta tunneling across the junction, a process known as a coherent quantum phase slip (QPS), can be obscured by unwanted capacitances when implemented using aluminum-based junctions. Superconducting constrictions that allow QPS's are a promising implementation that offer the possibility of qubits with stronger anharmonicities than their Al JJ-based counterparts[6], phase-slip oscillators that are highly sensitive and tunable via parametric drives[7], and a current standard based on QPSs[8]. Despite these proposed benefits, constriction-based QPS junctions have only been used in a handful of experiments[9–17]. This is in part due to the difficulty with fabricating narrow constrictions. Recent experiments have started to incorporate superconducting constrictions into quantum interference devices[15] and into circuits that could be used for metrology[16].

Incorporating constriction-based junctions into qubits would be particularly beneficial for quantum information processing. First, superconducting constrictions can be used to create qubits based on superpositions of persistent-current states[6] but without the need for incorporating shunting capacitors into the qubit circuit. Such qubit states are the basis for those used in the fluxonium[18], the bifluxon qubit[19], and the 0–π qubit[20,21]. The smaller parasitic capacitances enabled by superconducting constrictions are useful since capacitors lead to spurious modes that limit the operating frequency range and control mechanisms of the above-mentioned qubits. Second, it has

[1]Department of Physics, University of Illinois Urbana-Champaign, Urbana, IL, USA. [2]Holonyak Micro & Nanotechnology Lab, University of Illinois Urbana-Champaign, Urbana, IL, USA. [3]Dipartimento di Fisica, Sapienza Università di Roma, Rome, Italy. [4]Materials Research Laboratory, University of Illinois at Urbana-Champaign, Urbana, IL, USA. e-mail: akou@illinois.edu

been proposed that building a circuit that contains a junction acting as a tunneling element for flux quanta and a junction acting as a tunneling element for Cooper pairs could lead to a robust noise-protected qubit[22]. The lower shunting capacitances needed for implementing constriction-based QPS junctions significantly reduces the requirements for realizing such a circuit. Finally, constriction-based QPS qubits can be made from single films of higher-energy gap superconductors than aluminum. These qubits could have transition frequencies higher than those of current superconducting qubits, which would enable qubit operation above dilution refrigerator temperatures and would ease signal transduction between superconducting qubits and higher-energy quantum communication platforms such as optical photons. While GrAl-based qubits[17] are a promising pathway to realize devices with lower capacitances, they remain limited for use at high temperatures by the transition temperature of aluminum. It has been singularly challenging, however, to build non-Al constriction-based qubits[9,11]. Qubit frequencies could not be determined through design[9], and qubit coherence times were only inferred by spectroscopic linewidths[11].

In this work, we demonstrate the operation of a high-frequency superconducting qubit based on coherent QPSs tunneling through a superconducting constriction. We fabricate the qubit using a single thin film of TiN. The qubit is biased to zero flux, where the qubit basis states are similar to the recently-demonstrated bifluxon qubit[19,23,24], and the qubit frequency is mainly determined by the well-controlled qubit inductance. At this sweet spot, we demonstrate readout and coherent manipulation of the qubit. We observe qubit lifetimes in excess of 60 μs and qubit coherence times of ~17 ns. Finally, we exploit the higher-energy gap of TiN to operate the qubit at temperatures >300 mK. The relaxation and coherence times of the qubit remain robust, with T_{2R} unchanged and T_1 remaining above 10 μs, at these temperatures.

A phase-slip qubit is formed from an inductance in parallel with a QPS junction, which creates a superconducting loop as shown in Fig. 1a[6]. The eigenstates in a continuous superconducting loop are persistent-current states that correspond to quantized flux quanta in the loop. The addition of a QPS junction, here implemented as a constriction in the loop where quantum fluctuations of the superconducting order parameter are large, leads to flux quanta tunneling across the junction. While the QPS junction is sometimes discussed as an independent circuit element[9,22], we take here the point of view[25] that a constriction will behave as a QPS junction only if shunted by a circuit with the right impedance. If the constriction impedance dominates, then the current through the circuit will be determined by the tunneling rate of Cooper pairs across the constriction, resulting in the constriction acting as a JJ. If the loop impedance significantly exceeds that of the constriction, then a small circulating current determined mainly by the loop will flow through the entire circuit, and the constriction will act as a QPS junction. The resulting eigenstates of the circuit in the latter case are then coherent superpositions of different numbers of flux quanta in the loop. The normal state resistance of the superconducting loop in our device is larger than that of the constriction by two orders of magnitude (See Supplementary Information), indicating that our constriction acts as a QPS junction.

The phase-slip qubit is defined by the ground ($|g\rangle$) and first excited ($|e\rangle$) states of this device. By tuning the flux through the phase-slip circuit, Φ_{ext}, one can adjust the qubit energies and eigenstates as shown in Fig. 1d. Qubits based on phase slips have been implemented with Al-based JJs,[18,23,24,26], granular aluminum[17], and disordered superconductors[9,11]. The main difference between these implementations is the energies at which the phase-slip circuit shown in Fig. 1a no longer describes the device, and it becomes necessary to include the contribution of parasitic capacitances. Plasmon modes due to the capacitive contribution occur at a few GHz for circuits using Al-based JJs[18] but can be significantly higher in circuits using constrictions in disordered superconductors and granular aluminum[9,17]. In our device, we estimate that the first plasma mode occurs above 50 GHz (see Supplementary Information).

At integer and half-multiple flux quantum, qubit eigenstates are equal superpositions of flux quanta through the loop and become insensitive to dephasing from fluctuations in the flux through the phase-slip qubit. Previous implementations of constriction-based phase-slip qubits have been operated at half-flux quantum[9,11]. Half-flux quantum, however, is a difficult operating point for phase-slip qubits made using constrictions due to the exponential sensitivity of the qubit energy on the width of the constriction.

We focus instead on the integer-flux operating point of the phase-slip qubit. Here, the qubit energy remains insensitive to flux noise while also being only weakly dependent on the phase-slip rate through the QPS junction. The qubit frequency is primarily determined by E_L in the limit $E_L \gg E_{s,i}$, where $E_L = \Phi_0^2/L_k$ is the energy due to the inductance (L_k) of the loop and $E_{s,i}$ is the rate of i coherent quantum phase slips through the QPS junction. The inductive energy is controlled reliably through the inductance of the phase-slip qubit. $E_{s,i}$ determines the energy splitting between the first and second-excited ($|f\rangle$) states, which is a small perturbation on the qubit frequency. At integer flux, the qubit is thus minimally sensitive to the geometric parameters of the constriction. Moreover, the minimal overlap between the ground and excited state of the qubit eigenstates at integer flux provides increased protection against qubit relaxation[19,23,24].

Results

Our implementation of a phase-slip qubit is shown in Fig. 1b, c. The device is formed from a single layer of thin (5 nm thick) TiN, which was chosen due to its large kinetic inductance[27–29] and high measured quality factors[27,30]. We fabricated the junction from a narrow constriction of width ~18 nm (Fig. 1c), which is smaller than the expected coherence length of TiN to enable coherent QPSs through the constriction[31–33]. Since uncontrolled phase slips across the loop inductance are a detrimental dephasing process for the phase-slip qubit[34,35], we designed the width of the inductance to be 150 nm, which should be wide enough relative to the superconducting coherence length to prevent these spurious phase slips. The inductance is shown in green in Fig. 1b. We couple the phase-slip device inductively to a readout resonator in order to perform dispersive readout using standard circuit QED techniques[36]. We have measured two devices (A and B), which showed similar results. We will discuss Device A in the main text, while measurements from Device B can be found in the Supplementary Information.

We first performed two-tone spectroscopy on the device to check that it is behaving as a phase-slip qubit (Fig. 2). We expect the behavior of the device to be described by the following Hamiltonian written in the fluxon basis:

$$\begin{aligned} H = & \frac{E_L}{2}\sum_m [(m - \frac{\Phi_{\text{ext}}}{\Phi_0})^2 |m\rangle\langle m|] \\ & - \frac{E_{s,1}}{2}\sum_m (|m\rangle\langle m+1| + |m+1\rangle\langle m|) \\ & + \frac{E_{s,2}}{2}\sum_m (|m\rangle\langle m+2| + |m+2\rangle\langle m|) \end{aligned} \quad (1)$$

where m is the number of fluxons in the loop, $E_{s,1}$ is the phase-slip rate for coupling the fluxon states m and $m+1$, and $E_{s,2}$ is the rate at which two flux quanta tunnel simultaneously, coupling the fluxon states m and $m+2$. We fit both the $|g\rangle - |e\rangle$ and the $|g\rangle - |f\rangle$ transitions to the Hamiltonian described by Eq. (1) (solid lines in Fig. 2a) and observe good agreement between the data and theory. From the fit, we find $E_L = 34.4$ GHz, $E_{s,1} = 1.03$ GHz, and $E_{s,2} = 0.05$ GHz. Equation (1) is an effective low-energy Hamiltonian that only holds for our circuit up to

https://doi.org/10.1038/s41467-025-66348-w

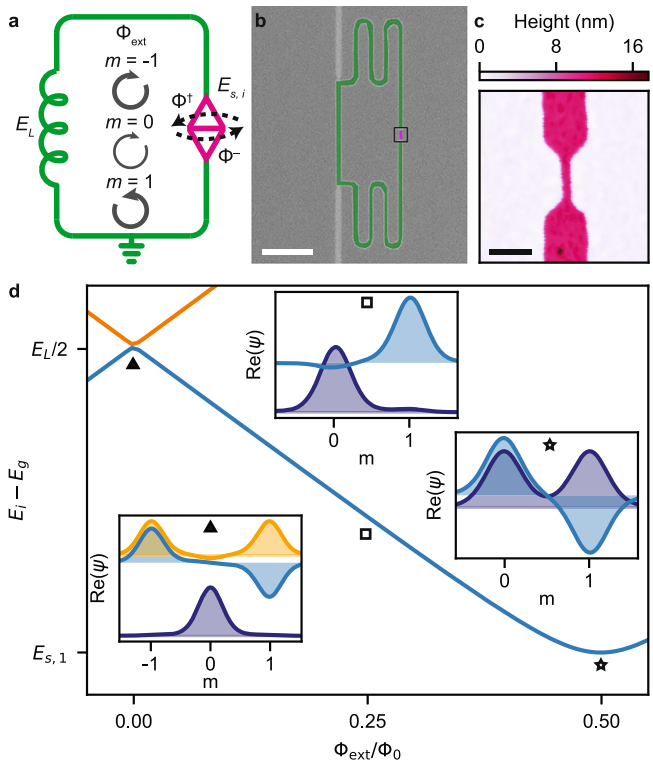

Fig. 1 | The phase-slip qubit. a Circuit schematic of the device. The superinductance (green) is in parallel with a superconducting constriction (pink) where flux quanta can tunnel into and out of the loop at a rate $E_{s,i}$. The arrows indicate the strength and chirality of the current in the loop for fluxon states, $m = -1, 0, 1$, when the external flux, Φ_{ext}, is slightly off of zero flux. **b** False-colored SEM image of lithographically similar device to Device A with the superinductance shown in green and the constriction shown in pink. The qubit is inductively coupled to a readout resonator (light gray). Scale bar corresponds to 5 µm. **c** Atomic force microscopy image of the 18 nm wide constriction forming the QPS junction. Scale bar corresponds to 100 nm. **d** Transition energy spectrum from the ground state of a phase-slip qubit as a function of Φ_{ext}. At zero flux, the qubit frequency is mainly determined by E_L, provided that $E_L \gg E_{s,i}$. The insets show the wavefunctions of the ground (navy), first (blue), and second-excited (orange) states at $\Phi_{ext} = 0$, 0.25 and 0.5 Φ_0.

the energy of the first plasmon mode. By fitting our data to the more general fluxonium Hamiltonian (fit parameters provided in Supplementary information), we find that the first plasmon mode is expected above 50 GHz, which indicates that Eq. (1) describes our experiments well. As an additional check that the qubit is behaving as predicted, we note that this Hamiltonian enforces a parity selection rule at exactly zero flux for transitions between the $|g\rangle$ and $|f\rangle$ state, which we observe as a decrease in the visibility of that transition.

We also demonstrate our ability to perform single-shot readout, which is essential in implementing future quantum algorithms and quantum error correction schemes. We drove the qubit at the $|g\rangle$-$|e\rangle$ frequency to populate the qubit in both the ground and excited states, and measured the resonator response. We performed this measurement 2×10^6 times and constructed a histogram of the resulting data, which is presented in Fig. 2b. We observe clear separation between the $|g\rangle$ and $|e\rangle$ resonator responses with an assignment fidelity of 96%[37].

We next perform qubit control by driving Rabi oscillations between the ground state and the excited state. We applied a drive with amplitude, A, and varied the duration, t, before measuring the state of the qubit via a readout pulse as described by the sequence shown in Fig. 2d. Figure 2c shows oscillations in the qubit state as a function of A and t. The extracted Rabi frequency for each pulse amplitude is plotted in Fig. 2e. The measured Rabi frequency depends linearly on the amplitude, which we expect for the behavior of a driven qubit. We note that despite the proximity of the $|g\rangle - |f\rangle$ transition to the $|g\rangle - |e\rangle$ transition, we do not observe any spurious oscillations in Fig. 2c. This further indicates that our phase-slip qubit is behaving as a well-controlled two-level system (TLS).

We conducted time-domain measurements to characterize the qubit lifetime and coherence at the zero flux sweet spot. We used standard measurement protocols to measure the relaxation time T_1, the Ramsey coherence time T_{2R}, and the single Hahn-echo coherence time T_{2E} (Fig. 3a–c). The observed T_1 improves upon previously measured relaxation times in phase-slip qubits at $\Phi_{ext} = 0.5\Phi_0$ by a factor of 10^3. The T_{2R} is significantly smaller than T_1, however, which indicates strong qubit dephasing. The coherence time only partly improves with an echo pulse, indicating that the qubit may be suffering from high-frequency noise. The echo may also have resulted in limited improvement because our X_π pulse was imperfect due to our pulse width being comparable to T_{2R}.

Next, we investigate the flux and time dependence of T_1 to identify the loss mechanisms affecting our phase-slip qubit (Fig. 3d). The relaxation time demonstrates well-defined flux dependence around zero flux, but fluctuates significantly as the flux is moved away from zero flux as shown in the inset of Fig. 3d. Near zero flux, we can model the flux dependence of the relaxation due to inductive loss[38] and find an inductive quality factor, $Q_{ind} = 4.2 \times 10^4$. We speculate that the inductive loss originates from material defects or excess quasiparticles in the superinductance[38]. The measured T_1 deviates significantly from the fit as we sweep away from zero Φ_0. From qubit spectroscopy in these regions, we suspect that the qubit may be coupling to multiple TLS, which would unpredictably degrade the relaxation time and contribute to this deviation. We have also measured T_1 over multiple days at zero flux and observed fluctuations from $T_1 = 40$–70 µs (shown in the multiple data points at zero flux in Fig. 3d). We conjecture that this variability could also be due to spurious TLS coupling to the qubit, with the TLS landscape changing over time[39].

Next, we performed T_{2R} measurements versus flux near zero flux to investigate the dephasing mechanisms of the qubit (Fig. 3e). We consider three contributions to dephasing: flux noise[40,41], Aharonov-Casher (AC) noise[34,35], and noise due to the proximity of the $|f\rangle$ state[23], depicted by the green, pink and orange lines in Fig. 3e, respectively. Flux noise contributes strongly to the dephasing away from zero flux, but the qubit becomes first-order insensitive to flux noise at zero flux. We thus expect the AC noise and thermal excitations of the $|f\rangle$ state to determine the coherence times at zero flux. Possible sources for AC noise may arise from localized charge puddles or excess quasiparticles in the disordered superconductor[42]. The slow dephasing from AC noise has typically been mitigated using echo sequences[35], but we do not observe a significant improvement in T_{2E} over T_{2R}. We therefore also consider fast dephasing due to the proximity of the $|f\rangle$ state. Since the $|f\rangle$ state is located only ~70 MHz away from the $|e\rangle$ state at zero flux, thermal excitation from $|e\rangle$ to $|f\rangle$ can cause dephasing[23]. Fitting our data using a quadrature sum of all three mechanisms (black line in Fig. 3e), we find a flux noise amplitude of $A_\Phi = 1.41 \times 10^{-4}\Phi_0/\sqrt{\text{Hz}}$, an AC noise amplitude, $A_{AC} = 0.026E_{s,1}/\sqrt{\text{Hz}}$, and a qubit temperature of 17 mK (from dephasing to the $|f\rangle$ state). The extracted A_Φ is ~ 2 orders of magnitude larger than current state-of-the-art JJ-based flux qubits[43]. Impurities introduced during device fabrication may be responsible for this increased flux noise[31]. The low extracted qubit temperature is surprising when compared with our qubit histogram measurements and previous experiments on superconducting qubits[17,44]. We hypothesize that changing the geometry of the constriction will enable us to better identify the contributions associated with each dephasing mechanism and reduce the total dephasing experienced by the qubit.

Finally, we investigate the benefits of the higher qubit frequency and larger gap of TiN in operating the phase-slip qubit at higher

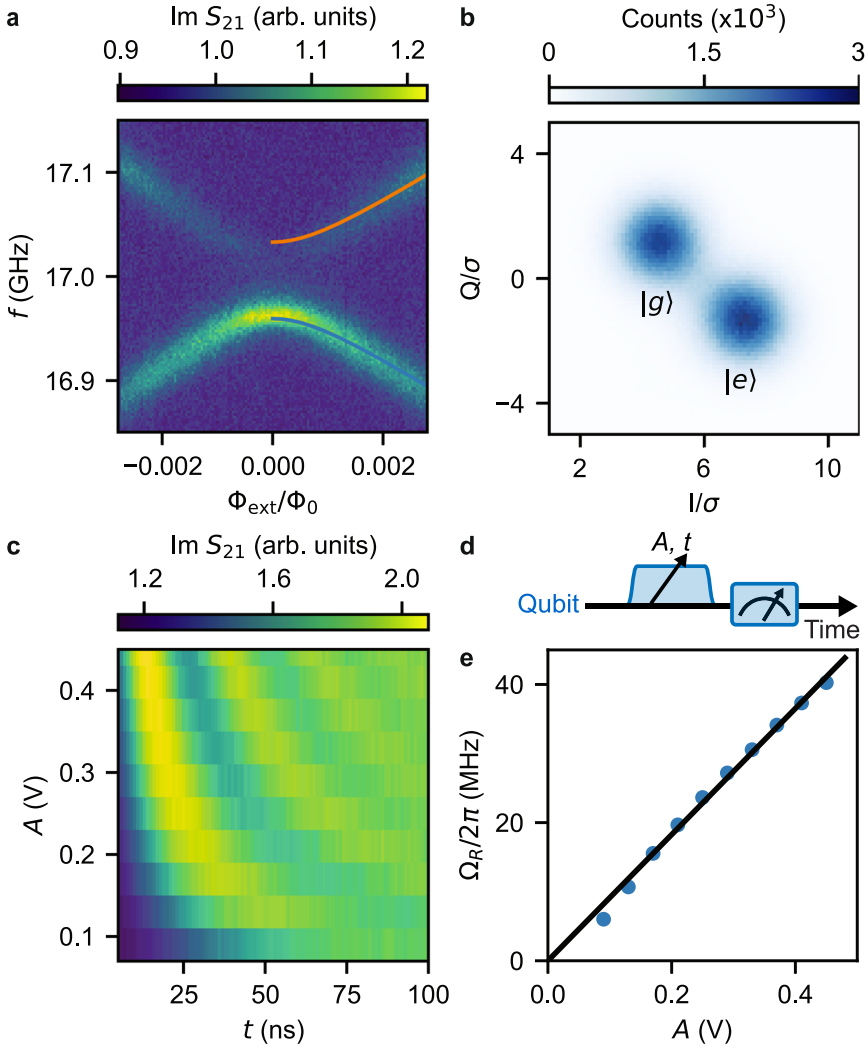

Fig. 2 | Qubit readout and control. a Two-tone spectroscopy near zero flux. The fit to the $|g\rangle$-$|e\rangle$ transition (blue line) and $|g\rangle$- $|f\rangle$ transition (orange line) is shown on the right half of the data. **b** Histogram of single-shot qubit readout. The qubit is populated to both the ground and excited state via a $X_{\pi/2}$ pulse prior to measurement. We read out the qubit at the resonator frequency corresponding to the qubit being in the $|g\rangle$ state. **c** Rabi oscillations of the qubit versus a square pulse with room temperature drive amplitude A and length t. **d** Pulse sequence for the Rabi experiment shown in (**c**). **e** Rabi frequency as a function of A. We extract the Rabi frequencies from (**c**). The black line is a linear fit of the Rabi frequency versus drive amplitude.

temperatures. Fig. 4a, b shows the measured relaxation time and coherence time of the qubit up to 385 mK. We observe that T_1 remains above 20 µs for temperatures up to 300 mK while T_{2R} remains essentially constant with temperature. The relaxation time shows a slow degradation up to 240 mK, after which T_1 decreases significantly. Previous measurements of aluminum-based superconducting qubits have also observed a significant decrease in T_1 at temperatures around 150 mK, which was attributed to an increase in quasiparticle loss[45–47]. More recent experiments have demonstrated that the operating temperature of Al JJ-based qubits could be increased by proximitizing the junction using Nb, but observed short lifetimes of ~1 µs for qubits operating at higher frequencies >10 GHz[48].

The decreased T_1 in our work is unexpected since the measured transition temperature of our TiN film is 2.9 K. We additionally measured the qubit excited-state population as a function of temperature to better understand the temperature dependence of the relaxation time as shown in Fig. 4c. In the qubit histograms for these measurements, we observe two separated resonator responses corresponding to the $|g\rangle$ and $|e\rangle$ states. The measured probability from these histograms is converted to qubit temperature using the Boltzmann distribution (right axis in Fig. 4c). The qubit temperature appears to be consistently greater than the mixing chamber temperature by >100 mK. We note that due to the fast decay rate of $|f\rangle$ to $|e\rangle$, we may be overestimating the $|e\rangle$ population in our readout histograms due to thermal population of $|f\rangle$. This possible overestimation is reflected in the lower bound of the error bars in Fig. 4c for the qubit temperature and population data. Using the measured qubit temperature, we model the reduction in lifetime as inductive loss, with Q_{ind} changing as a function of qubit temperature to reflect an increasing quasiparticle density as shown by the gray points with dashed lines in Fig. 4a (See Supplementary Information). We find reasonable agreement of the measured relaxation times with this model.

Discussion

We have demonstrated all essential single-qubit functions in a phase-slip qubit operated at zero flux, fabricated from a single layer of TiN. Our results show that a superconducting constriction is a viable alternative source of nonlinearity that can be used in coherent quantum devices. Having multiple superconducting sources of nonlinearity significantly expands the possible quantum coherent devices that can be built. First, since the QPS junction effectively behaves as a nonlinear capacitor rather than a nonlinear inductor (up to an expected frequency of 53 GHz in our case), it would allow for the creation of novel oscillators with photon-dependent non-linearities[7] that can be used for

https://doi.org/10.1038/s41467-025-66348-w

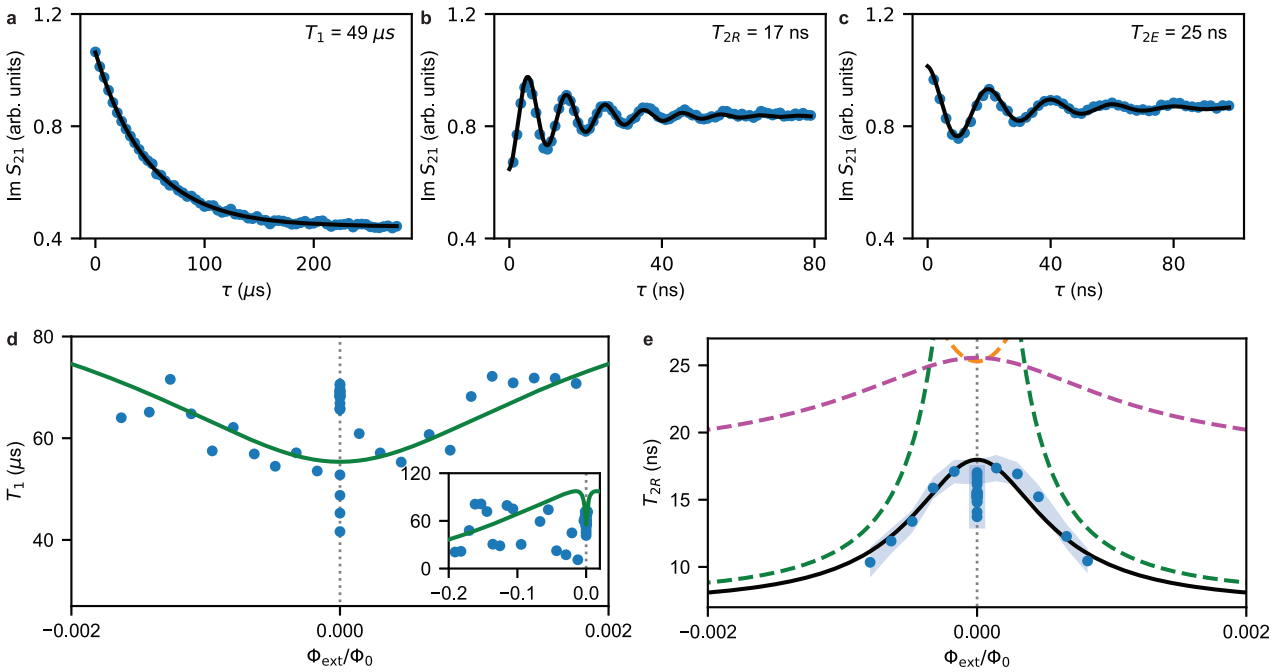

Fig. 3 | Qubit relaxation and coherence. a–c Time-domain measurements taken at zero flux, measuring **a** the relaxation time T_1, **b** the Ramsey coherence time T_{2R}, and **c** the coherence time with the application of a single echo pulse T_{2E}. The duration of the X_π and $X_{\pi/2}$ pulses used in the measurements was 9 ns. **d** Relaxation time T_1 versus flux. The expected flux dependence of T_1 due to inductive loss with $Q_{ind} = 4.2 \times 10^4$ is plotted in green. The inset shows that T_1 deviates from the inductive loss fit away from zero flux. The gray dotted line is a guide for the eye for zero flux. The range of variations of T_1 in time is shown by the data points at zero flux. **e** Ramsey coherence time T_{2R} versus flux. The shaded region indicates the error from fitting the T_{2R} data. The dashed lines indicate the individual contributions to the dephasing of the qubit. The green line shows the expected flux dependence of T_{2R} due to first-order flux noise dephasing with noise amplitude, $A_\Phi = 1.41 \times 10^{-4}\Phi_0/\sqrt{\text{Hz}}$, the pink line is the limit set by Aharonov-Casher dephasing for variation in $E_{s,1}$ with noise amplitude, $A_{AC} = 0.026E_{s,1}/\sqrt{\text{Hz}}$, the orange line indicates the limit set by thermal excitations to the $|f\rangle$ state for a qubit temperature of 17 mK. The black line shows the expected limit from the quadrature sum of all three contributions. Similar to **d**, the gray line is a guide for zero flux, and the range of variations of T_{2R} in time is shown by the data points at zero flux. Note that at zero flux, only the point with the highest T_{2R} was included in the fit.

sensitive detection and signal amplification. Second, TiN has been demonstrated to have higher quality factors than evaporated aluminum[27]. Our demonstrated phase-slip qubit is thus a first step toward qubits with longer possible relaxation times than current AlOx-junction-based superconducting qubits. Achieving longer qubit coherence times will be necessary for the constriction-based phase-slip qubit to become a competitive platform for quantum information processing. While our qubit has relaxation times comparable to standard JJ-based superconducting qubits, the coherence times of the qubit are very short. Improved cleaning methods in the device processing or changes in the geometry to reduce the sensitivity of phase-slip tunneling processes to fluctuating charges will further elucidate these decoherence mechanisms.

Our phase-slip qubit also presents a platform for building high-frequency qubits that can operate at high temperatures. Building superconducting qubits that can operate at high temperatures has become increasingly important as superconducting quantum processors run into limits imposed by the cooling capabilities of current technologies. While we observed that the qubit relaxation time started to degrade significantly at temperatures below the superconducting transition temperature, our demonstrated qubit operation above 100 mK already significantly reduces the technological requirements needed to cool superconducting qubits beyond what can be achieved by aluminum-based superconducting qubits. The observed poor thermalization of the qubit may be due to its coupling to a different bath compared with current superconducting qubits, which would require additional filtering compared to standard devices. The very thin superconducting TiN film may also have large enough disorder to prolong thermalization times; measurements of qubits made using superconducting films with different levels of disorder will be useful in understanding this mechanism. Usage of superconducting films with even higher transition temperatures than TiN may present a path to superconducting qubits operating above 4K.

Methods

Device fabrication

We fabricated the sample from a 5-nm-thick TiN film on a 720 μm-thick silicon substrate. Smaller features such as the resonator and the qubit were fabricated using electron-beam lithography (Elionix ELS-G150) with ZEP 520A resist. We used photolithography (Heidelberg MLA 150) with AZ1518 resist to pattern larger features such as the ground plane and transmission line. The sample was etched after each patterning step using an Oxford Mixed ICP-RIE system with a chemistry of Cl_2, BCl_3, and Ar. To clean the sample, we used an O_2 descum process, followed by rinsing in N-Methylpyrrolidone. Prior to wirebonding to a printed circuit board, the sample was rinsed in buffered oxide echant to remove surface oxides.

Experimental setup

The sample was enclosed in a Copper sample holder and cooled to 10 mK in a dilution refrigerator (Oxford Instruments, Triton 500). A coil was mounted to the sample holder, and a DC current source (Yokogawa, GS200) was used to apply a magnetic field to the sample. The readout and qubit pulses were formed by mixing local oscillator tones from signal generators with IQ tones from an integrated FPGA system (Quantum Machines, OPX+). The input signal was thermalized via attenuators at different temperature plates before reaching the mixing chamber. At the mixing chamber plate, the input was sent

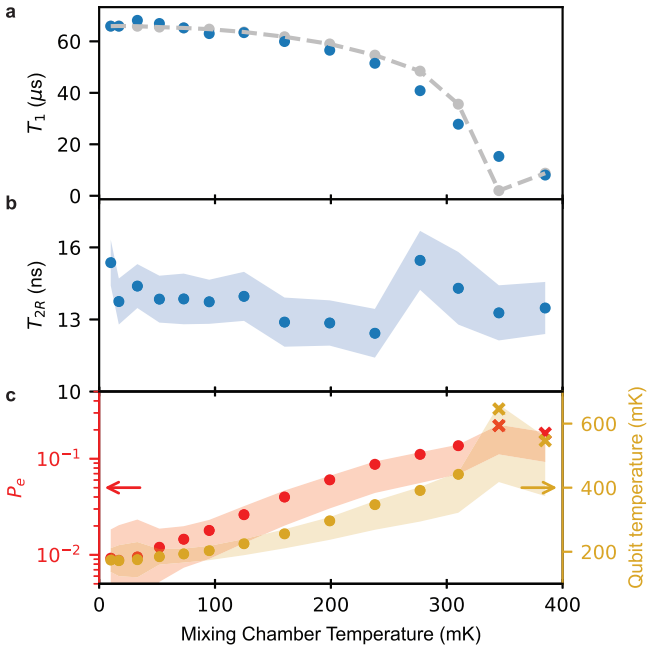

Fig. 4 | Operation of the qubit at elevated temperatures. a Temperature dependence of qubit lifetime. The blue points are the measured T_1 values. The gray points with dashed lines represent the expected T_1 degradation due to decreasing Q_{ind} from the rise in the quasiparticle population as the qubit temperature increases. We use the measured qubit temperature as input to our model. **b** Temperature dependence of qubit coherence time. The shaded region is the error from the T_{2R} fit. T_{2R} does not show significant variation with temperature. **c** Excited-state probability, P_e (left) and qubit temperature (right) as a function of mixing chamber temperature. The upper bound of the shaded region represents the uncertainty from the qubit histogram fit. The lower bound of the shaded region also accounts for the uncertainty associated with overestimating the $|e\rangle$ state population due to excess $|f\rangle$ state population in the qubit histogram. The crosses represent data which was taken with a different readout parameter compared to the circles, which were chosen due to the reduction in T_1 at higher temperatures.

through an Eccosorb filter to filter out high-frequency noise before entering the transmission line.

The output from the transmission line was routed through another Eccosorb filter followed by a traveling-wave parametric amplifier. The output signal was then amplified again at the 4K plate via a high-electron-mobility transistor amplifier (Low Noise Factory, LNF-LNC4_16B) and at room temperature via a low noise amplifier (LNF-LNR4_14B_SV). The signal was demodulated and further amplified before being sent to the FPGA for processing.

Simulations

Prior to measurements, we estimated the resonator frequency and coupling quality factor using electromagnetic field simulations (Ansys HFSS). To solve the Hamiltonian and estimate the qubit frequency, we employed numerical diagonalization using QuTip[49]. We also used QuTip to fit the qubit spectroscopy and perform master equation pulse-level simulations (See Supplementary Information).

Data availability

The experimental data that support the findings of this study are available in the Illinois Data Bank at https://doi.org/10.13012/B2IDB-0982994_V2[50].

Code availability

The code used for the data analysis and visualization is available at is available in the Illinois Data Bank at https://doi.org/10.13012/B2IDB-0982994_V2[50].

References

1. Yurke, B. et al. Observation of parametric amplification and deamplification in a Josephson parametric amplifier. *Phys. Rev. A* **39**, 2519–2533 (1989).
2. Macklin, C. et al. A near-quantum-limited Josephson traveling-wave parametric amplifier. *Science* **350**, 307–310 (2015).
3. Walsh, E. D. et al. Josephson junction infrared single-photon detector. *Science* **372**, 409–412 (2021).
4. Kjaergaard, M. et al. Superconducting qubits: current state of play. *Annu. Rev. Condens. Matter Phys.* **11**, 369–395 (2020).
5. Krantz, P. et al. A quantum engineer's guide to superconducting qubits. *Appl. Phys. Rev.* **6**, 021318 (2019).
6. Mooij, J. E. & Harmans, C. J. P. M. Phase-slip flux qubits. *N. J. Phys.* **7**, 219–219 (2005).
7. Hriscu, A. M. & Nazarov, Y. V. Model of a proposed superconducting phase slip oscillator: a method for obtaining few-photon nonlinearities. *Phys. Rev. Lett.* **106**, 077004 (2011).
8. Mooij, J. E. & Nazarov, Y. V. Superconducting nanowires as quantum phase-slip junctions. *Nat. Phys.* **2**, 169–172 (2006).
9. Astafiev, O. V. et al. Coherent quantum phase slip. *Nature* **484**, 355–358 (2012).
10. Potter, J., Fenton, J. & Warburton, P. Controllable tunneling of single flux quanta mediated by quantum phase slip in disordered superconducting loops. *Phys. Rev. Appl.* **19**, 024002 (2023).
11. Peltonen, J. T. et al. Coherent dynamics and decoherence in a superconducting weak link. *Phys. Rev. B* **94**, 180508 (2016).
12. Hönigl-Decrinis, T. et al. Capacitive coupling of coherent quantum phase slip qubits to a resonator. *N. J. Phys.* **25**, 113020 (2023).
13. Peltonen, J. T. et al. Coherent flux tunneling through NbN nanowires. *Phys. Rev. B* **88**, 220506 (2013).
14. Belkin, A., Belkin, M., Vakaryuk, V., Khlebnikov, S. & Bezryadin, A. Formation of quantum phase slip pairs in superconducting nanowires. *Phys. Rev. X* **5**, 021023 (2015).
15. De Graaf, S. E. et al. Charge quantum interference device. *Nat. Phys.* **14**, 590–594 (2018).
16. Shaikhaidarov, R. S. et al. Quantized current steps due to the a.c. coherent quantum phase-slip effect. *Nature* **608**, 45–49 (2022).
17. Rieger, D. et al. Granular aluminium nanojunction fluxonium qubit. *Nat. Mater.* **22**, 194–199 (2023).
18. Manucharyan, V. E., Koch, J., Glazman, L. I. & Devoret, M. H. Fluxonium: single cooper-pair circuit free of charge offsets. *Science* **326**, 113–116 (2009).
19. Kalashnikov, K. et al. Bifluxon: fluxon-parity-protected superconducting qubit. *PRX Quantum* **1**, 010307 (2020).
20. Brooks, P., Kitaev, A. & Preskill, J. Protected gates for superconducting qubits. *Phys. Rev. A* **87**, 052306 (2013).
21. Gyenis, A. et al. Experimental realization of a protected superconducting circuit derived from the 0 - π qubit. *PRX Quantum* **2**, 010339 (2021).
22. Le, D. T., Grimsmo, A., Müller, C. & Stace, T. M. Doubly nonlinear superconducting qubit. *Phys. Rev. A* **100**, 062321 (2019).
23. Ardati, W. et al. Using bifluxon tunneling to protect the fluxonium qubit. *Phys. Rev. X* **14**, 041014 (2024).
24. Mencia, R. A., Lin, W.-J., Cho, H., Vavilov, M. G. & Manucharyan, V. E. Integer fluxonium qubit. *PRX Quantum* **5**, 040318 (2024).
25. Vanević, M. & Nazarov, Y. V. Quantum phase slips in superconducting wires with weak inhomogeneities. *Phys. Rev. Lett.* **108**, 187002 (2012).
26. Mooij, J. E. et al. Josephson persistent-current qubit. *Science* **285**, 1036–1039 (1999).
27. Amin, K. R. et al. Loss mechanisms in TiN high impedance superconducting microwave circuits. *Appl. Phys. Lett.* **120**, 164001 (2022).
28. Joshi, C., Chen, W., LeDuc, H. G., Day, P. K. & Mirhosseini, M. Strong kinetic-inductance Kerr nonlinearity with titanium nitride nanowires. *Phys. Rev. Appl.* **18**, 064088 (2022).

29. Shearrow, A. et al. Atomic layer deposition of titanium nitride for quantum circuits. *Appl. Phys. Lett.* **113**, 212601 (2018).
30. Vissers, M. R. et al. Low loss superconducting titanium nitride coplanar waveguide resonators. *Appl. Phys. Lett.* **97**, 232509 (2010).
31. Saveskul, N. et al. Superconductivity behavior in epitaxial Ti N films points to surface magnetic disorder. *Phys. Rev. Appl.* **12**, 054001 (2019).
32. Faley, M. I., Liu, Y. & Dunin-Borkowski, R. E. Titanium nitride as a new prospective material for NanoSQUIDs and superconducting nanobridge electronics. *Nanomaterials* **11**, 466 (2021).
33. Bastiaans, K. M. et al. Direct evidence for Cooper pairing without a spectral gap in a disordered superconductor above T_c. *Science* **374**, 608–611 (2021).
34. Manucharyan, V. E. et al. Evidence for coherent quantum phase slips across a Josephson junction array. *Phys. Rev. B* **85**, 024521 (2012).
35. Randeria, M. T. et al. Dephasing in fluxonium qubits from coherent quantum phase slips. *PRX Quantum* **5**, 030341 (2024).
36. Blais, A. et al. Quantum-information processing with circuit quantum electrodynamics. *Phys. Rev. A* **75**, 032329 (2007).
37. Gambetta, J., Braff, W. A., Wallraff, A., Girvin, S. M. & Schoelkopf, R. J. Protocols for optimal readout of qubits using a continuous quantum nondemolition measurement. *Phys. Rev. A* **76**, 012325 (2007).
38. Smith, W. C., Kou, A., Xiao, X., Vool, U. & Devoret, M. H. Superconducting circuit protected by two-Cooper-pair tunneling. *npj Quantum Inf.* **6**, 1–9 (2020).
39. Thorbeck, T., Eddins, A., Lauer, I., McClure, D. T. & Carroll, M. Two-level-system dynamics in a superconducting qubit due to background ionizing radiation. *PRX Quantum* **4**, 020356 (2023).
40. Koch, R. H. et al. Flicker (1/f) noise in tunnel junction dc SQUIDS. *J. Low. Temp. Phys.* **51**, 207–224 (1983).
41. Ithier, G. et al. Decoherence in a superconducting quantum bit circuit. *Phys. Rev. B* **72**, 134519 (2005).
42. De Graaf, S. E. Dual Fraunhofer interference and charge fluctuations in long quantum phase slip wires. *Phys. Rev. B* **102**, 144509 (2020).
43. Nguyen, L. B. et al. High-coherence fluxonium qubit. *Phys. Rev. X* **9**, 041041 (2019).
44. Bao, F. et al. Fluxonium: an alternative qubit platform for high-fidelity operations. *Phys. Rev. Lett.* **129**, 010502 (2022).
45. Paik, H. et al. Observation of high coherence in Josephson junction qubits measured in a three-dimensional circuit QED architecture. *Phys. Rev. Lett.* **107**, 240501 (2011).
46. Serniak, K. et al. Hot nonequilibrium quasiparticles in transmon qubits. *Phys. Rev. Lett.* **121**, 157701 (2018).
47. Martinis, J. M., Ansmann, M. & Aumentado, J. Energy decay in superconducting Josephson-junction qubits from nonequilibrium quasiparticle excitations. *Phys. Rev. Lett.* **103**, 097002 (2009).
48. Anferov, A., Harvey, S. P., Wan, F., Simon, J. & Schuster, D. I. Superconducting qubits above 20 GHz Operating over 200 mK. *PRX Quantum* **5**, 030347 (2024).
49. Johansson, J., Nation, P. & Nori, F. QuTiP 2: a python framework for the dynamics of open quantum systems. *Comput. Phys. Commun.* **184**, 1234–1240 (2013).
50. Purmessur, C., Chow, K., van Heck, B. & Kou, A. Data for: operation of high frequency, phase slip qubit. Illinois Data Bank, https://doi.org/10.13012/B2IDB-0982994_V2 (2025).

Acknowledgements

We thank Matthias Steffen, Benjamin Wymore, Oliver Dial, Aayam Bista, Xi Cao, Jared Gibson, Jinwoong Philip Kim, Michael Mollenhauer, Ke Nie, and Randy Owen for useful discussions. The TiN film and traveling-wave parametric amplifier used in this experiment were provided by IBM. This research was conducted in part at the Materials Research Lab Central Facilities and the Holonyak Micro and Nanotechnology Lab, University of Illinois. C.P. and A.K. are funded through the IBM-Illinois Discovery Accelerator Institute.

Author contributions

C.P. designed and measured the devices. K.C. and C.P. fabricated the devices. C.P. performed the data analysis with input from B.v.H. and A.K. C.P. and A.K. wrote the manuscript, with feedback from all authors. A.K. conceived and supervised the experiment.

Competing interests

The authors declare no competing interests.

Additional information

Supplementary information The online version contains supplementary material available at https://doi.org/10.1038/s41467-025-66348-w.

Correspondence and requests for materials should be addressed to Angela Kou.

Peer review information *Nature Communications* thanks the anonymous reviewers for their contribution to the peer review of this work.